

An experimental study of a quasi-impulsive backwards wave force associated with secondary load cycle on a vertical cylinder

Tianning Tang¹, Haoyu Ding², Saishuai Dai³, Paul H. Taylor⁴, Jun Zang² and Thomas A. A. Adcock¹

¹Department of Engineering Science, University of Oxford, Oxford, OX1 3PJ, UK

²Department of Architecture and Civil Engineering, University of Bath, Bath, BA2 7AY, UK

³Naval Architecture, Ocean and Marine Engineering Department,
University of Strathclyde, Glasgow, G1 1XQ, UK

⁴Oceans Graduate School, The University of Western Australia,
35 Stirling Highway, Crawley, WA 6009, Australia

(Received xx; revised xx; accepted xx)

Steep wave breaking on vertical cylinder (a typical foundation supporting offshore wind turbines) will induce slam loads. Many questions on the important violent wave loading and the associated secondary load cycle still remain unanswered. We use laboratory experiments with unidirectional waves to investigate the fluid loading on vertical cylinders. We use a novel three-phase decomposition approach which allows us to separate different types of non-linearity. Our findings reveal the existence of an additional quasi-impulsive loading component that is associated with the secondary load cycle and occurs in the backwards direction against that of the incoming waves. This quasi-impulsive force occurs at the end of the secondary load cycle and close to the passage of the downward zero-crossing point of the undisturbed wave. Wavelet analysis showed that the impulsive force exhibits superficially similar behaviour to a typical wave-slamming event but in the reverse direction. To monitor the scattered wave field and extract run-up on the cylinder, we installed a four-camera synchronized video system and found a strong temporal correlation between the arrival time of the Type-II scattered wave onto the cylinder and the occurrence of this quasi-impulsive force. The temporal characteristics of this quasi-impulsive force can be approximated by the Goda wave impact model, taking the collision of the Type-II scattered waves at the rear stagnation point as the impact source.

Key words: Wave-structure interactions, Wave scattering

1. Introduction

The design of offshore structures requires accurate estimation of nonlinear wave loading. At the time of writing, monopiles are the most common form of support structure for offshore wind turbines which has led to renewed interest in the classical problem of wave loading on columns. MacCamy & Fuchs (1954) solved the linear problem many years ago with the focus since then being on the non-linear physics of the problem. The non-linear loading can be divided into two parts. Weak non-linearity, where the wave does not break, typically generates loads at harmonics of the fundamental incoming wave. For

instance, Chaplin *et al.* (1992) looked at the local forces on such a cylinder in regular and irregular waves. Loads from other processes which are usually only active above some critical steepness, for instance, loads from breaking waves or the secondary load cycle, can be considered strongly non-linear (Chella *et al.* 2012). Here we consider cylinders sufficiently large that drag forces play only a minor role.

Various second-order analytical and numerical models exist (e.g. Eatock Taylor & Hung (1987); Kim & Yue (1989); Chau & Eatock Taylor (1992)) and the third harmonic force was explored by Faltinsen *et al.* (1995); Malenica & Molin (1995); Newman (1996). The recent analytic work from Taylor *et al.* (2024) has derived a transformation of the third-order FNV theory, which uses only nonlinear surface elevation as input. These and higher harmonics have been studied by various authors such as Huseby & Grue (2000); Riise *et al.* (2018*a*) in experiments and computations. Recently, Chen *et al.* (2018); Tang *et al.* (2024) have developed a Stokes-type predictive model for the loading which has recently been extended to directional seas (Mj *et al.* 2023).

Steep waves breaking on a cylinder will induce slam loads (Sheikh & Swan 2005; Masterton & Swan 2006), for which a variety of models exist (Von Karman 1929; Wagner 1932; Ghadirian & Bredmose 2019). The wave-in-deck loads have further been explored by Ma & Swan (2020, 2023*a,b*), where loads are found to be critically dependent upon both the wave shape and the water particle kinematics. The interaction between these waves and the cylinder may create additional strongly non-linear loading, for instance, from the secondary load cycle, which appears between the passage of the crest and the following trough of the wave. This strongly nonlinear loading was first reported by Grue *et al.* (1993) and has been further explored in numerous studies of regular wave trains (Grue & Huseby 2002; Saincher *et al.* 2022; Wang *et al.* 2020), focused wave groups (Chaplin *et al.* 1997), and irregular sea states (Stansberg *et al.* 1995; Stansberg 1997), and also in multidirectional waves (Chaplin *et al.* 1993, 1995). Li *et al.* (2022) also deployed the Empirical Mode Decomposition (EMD) method to isolate the secondary load cycle, and Lee *et al.* (2021) proposed an empirical formulation to predict the occurrence of the secondary load cycle with regular wave experiments. The related scatter wave field has also been explored by Swan *et al.* (2005); Swan & Sheikh (2015) with tank experiments. The potential mechanisms underlying the secondary load cycle have been extensively discussed in the literature, including works by Tromans *et al.* (2006); Paulsen *et al.* (2014); Riise *et al.* (2018*b*) and also recently by Antolloni *et al.* (2020); Ghadirian & Bredmose (2020), where a suction behind the cylinder is believed to be closely associated with the presence of the secondary load cycle. However, the exact process that triggers the secondary load cycle remains unclear (Chang *et al.* 2019; Li *et al.* 2022).

Additionally, several of these studies reported structural resonant response at the natural frequency triggered by the secondary load cycle (Rainey 2007; Esandi *et al.* 2020), which can have detrimental effects on offshore structures. This structural resonant response is also commonly being referred as the “ringing” response of the offshore wind turbine in various literature (Marthinsen *et al.* 1996; Grue *et al.* 1994; Krokstad *et al.* 1998; Grue 2002; Zang *et al.* 2010; Liu & Teng 2023), which can also be triggered by higher-harmonic wave forces (Grue & Huseby 2002) as well as wave breaking (Choi *et al.* 2015; Ma & Swan 2020).

In this paper, we report a quasi-impulsive force associated with the secondary load cycle in the opposite direction to the incoming waves. This backwards force can be identified with the wavelet analysis method shown in Figure 1. The wavelet transform shows the spatial-temporal energy distribution of the nonlinear forcing on the vertical cylinder and enables us to investigate energy change in a short time scale. From Figure 1, this backwards force appears towards the end of the secondary load cycle (indicated by the

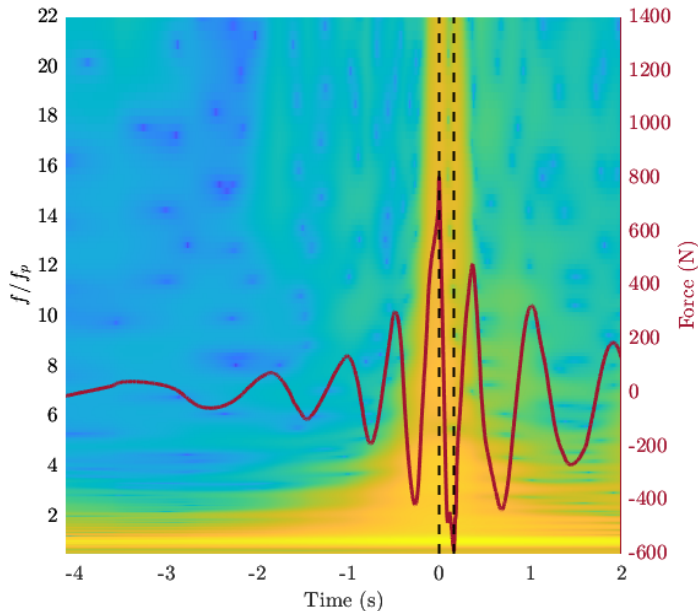


FIGURE 1. A demonstration of additional higher-frequency forces associated with secondary load cycle with wavelet analysis

second black dash line), and its frequency-temporal distribution of energy is superficially similar to the first impact due to wave breaking –having a wide range of high-frequency content (up to over $20 \times f_p$ the frequency of the wave spectral peak) and a very short duration (usually less than 0.1 seconds at lab scale). In past studies, this impulsive force was commonly regarded as a component of the secondary load cycle (Riise *et al.* 2018*b*). In this paper, however, we find this impulsive force to be an extra nonlinear process happening at the later stage of a secondary load cycle, and occurring at a slightly higher Froude number than the typical secondary load cycle reported previously. As such, the main focus of this study is on this extra nonlinear process, which excludes the initial part of the secondary load cycle.

To further investigate the quasi-impulsive force, we utilise a novel version of four phase decomposition Fitzgerald *et al.* (2014), using three of the four phase time histories to re-create what would have occurred in the fourth phase if the secondary load cycle had not occurred. This allows a clean separation of the secondary load cycle from the Stokes-type higher frequency load components. We explore the source of this impact from the scattered wave field using run-up profiles on the cylinder based on the synchronised videos in experiments. We confirm a strong correlation between this quasi-impulsive force with the previously reported Type-II scattered wave in Swan & Sheikh (2015). We note that, however, previous work primarily focused on the scattered wave effect at the front face of the cylinder sometime after the main interaction. We compare our findings with highly resolved CFD simulations and propose an engineering model to capture the main features of this quasi-impulsive force.

This paper is structured as follows. In Section 2 and 3, we introduce the experimental and numerical setups, respectively. In Section 4, we detail the methods used for exploring the underlying physical processes. The results are presented in Section 5, followed by discussions and conclusions in Section 6.

TABLE 1. Incoming wave group parameters for the experiments and numerical simulations. A_L is the maximum crest amplitude at focus as if the wave group evolved linearly, T_p is the peak wave period, d is water depth, k_p is the peak wave number associated with the peak wave period, R is cylinder radius.

Case	A_L (m)	T_p (s)	Method	$k_p R$	$k_p d$	$k_p A_L$
Case 1	0.28	2.56	Experiment	0.12	1.10	0.18
Case 2	0.23	1.85	Experiment	0.23	2.11	0.26
Case 3	0.35	2.52	Numerical Simulation	0.15	1.31	0.25
Case 4	0.29	2.52	Numerical Simulation	0.15	1.31	0.21

2. Experimental Setup

We performed experiments in the large towing tank (76 m long, 4.6 m wide with water depth set to 1.8m) at the Kelvin Hydrodynamics Laboratory, the University of Strathclyde (Figure 2). The tank in this study has a 14 m long passive sloping type beach at one end for wave absorption, the typical reflection coefficient from the beach is less than 5%. At the other end of the tank, there installed a state-of-the-art force-controlled active absorbing flap type wavemaker, designed and manufactured by Edinburgh Design Ltd. In this study, we focus on focused wave groups, where the reflected waves can simply excluded from the analysis by ignoring the time series after the wave group passes by. Based on linear wave generation theory, the wave maker is capable of providing a precision uncertainty of only 0.2%. A single surface-piercing vertical cylinder with a radius (R) of 0.2 m and fixed at both ends, was placed 35.3 m away from the wavemaker. A hammer test found the natural frequency to be 8 Hz corresponding to about $20.1 f_p$ and $14.8 f_p$ for two experimental cases presented herein, where f_p is the frequency with the peak spectral energy for the wave groups tested.

In this study, we generated uni-directional focused wave groups based on a JONSWAP spectrum following Young (2020) with a peak enhancement factor $\gamma = 3.3$, and generated a wide range in the nondimensionalised parameter space with $k_p R$ ranging from 0.1 to 0.55, and $k_p \eta_c$ from 0.05 to 0.42 with detailed parameters shown in Figure 7 (k_p being the wavenumber associated with frequency f_p , and is estimated according to finite wave depth linear dispersion relationship $(2\pi f_p)^2 = gk_p \tanh(k_p d)$, where d is water depth). The relative water depth $k_p d$ associated with these wave groups ranged from 1.2 to 3.8, giving intermediate to deep water conditions. Nonlinear wave evolution is expected for steep wave groups as the wave group propagates towards the cylinder (Lo & Mei 1985; Baldock *et al.* 1996; Adcock & Taylor 2009). As such, we recorded the local undisturbed properties of wave groups at the position of the centre of the cylinder by repeating the experiment without the presence of the cylinder and using these results as the undisturbed incident waves. The detailed parameters for two experimental and two numerically simulated cases are presented in Table 1.

We also use a four-camera system synchronised with the data acquisition system, to monitor the scattered wave field around the cylinder. The frame rate of these cameras is 20 fps and a check-board grid was wrapped around the cylinder with the size of each rectangle to be 50 mm in width and 49 mm in height. These synchronised cameras provide a detailed view of the scattered wave field and allow direct extraction of the run-up profile on the cylinder.

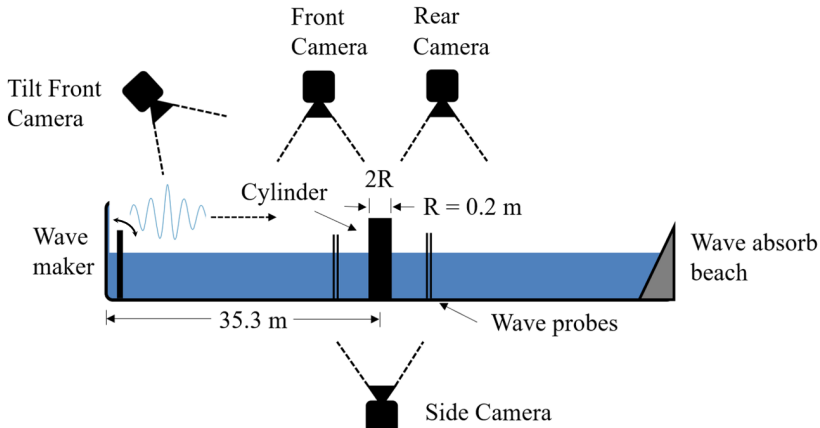


FIGURE 2. Experimental setup and synchronised camera system for experiments at Kelvin Hydrodynamics Laboratory, the University of Strathclyde.

3. Numerical Setup

We utilise a computational fluid dynamics model, OpenFOAM, based on the Navier-Stokes equations, in this research. A multi-phase solver, *interFoam*, is employed to simulate the wave-cylinder interactions with a volume of fluid method tracking the boundary interface between water and air. The $k - \omega$ SST model is used for turbulence modelling.

The numerical wave tank in OpenFOAM uses the same lateral and vertical dimensions as the physical experiments, as shown in Figure 3. The width of the numerical wave tank is 4.6 m, and the water depth remains constant at 1.8 m. The cylinder is installed in the middle of the wave tank. Two relaxation zones are defined in both *inlet* and *outlet* boundaries. The relaxation zone in the *inlet* boundary absorbs the reflected waves from the cylinder, while the other relaxation zone in the *outlet* boundary absorbs the incoming waves and suppresses wave reflection. Both relaxation zones are $1.5 \times$ the incoming wavelength, which is the recommended length by Jacobsen *et al.* (2012) for complete wave attenuation. Due to the setup of the relaxation zones, the total length of the numerical wave tank can be significantly shorter than the physical wave tank and without the influence of reflected waves. The total length of the wave tank is $7 \times$ the incoming wavelength. The incoming waves are generated by defining the wave parameters in the inlet boundary with the *waves2foam* toolbox (Jacobsen *et al.* 2012).

The mesh around the cylinder in OpenFOAM is also shown in Figure 3. Chen *et al.* (2014) conducted a series of mesh convergence tests to determine the appropriate mesh size to predict wave-cylinder interactions accurately. We adopt the same design for the outermost layer of mesh cells with $\Delta x = \Delta y = L/140$ and $\Delta z = A/8$, where Δx and Δy are the horizontal mesh size highlighted in Figure 3, Δz is the vertical mesh size, L is the incoming wavelength and A is the incoming wave amplitude. In this work, we refine the thickness, i.e., the horizontal width Δx , of the innermost layer around the cylinder further to $0.2 \times$ the thickness of the outermost layer to capture complex and highly localised wave behaviours, such as steep gradient of wave run-up on the cylinder and the secondary load cycle. The detailed parameters of the simulation cases are presented in Table 1.

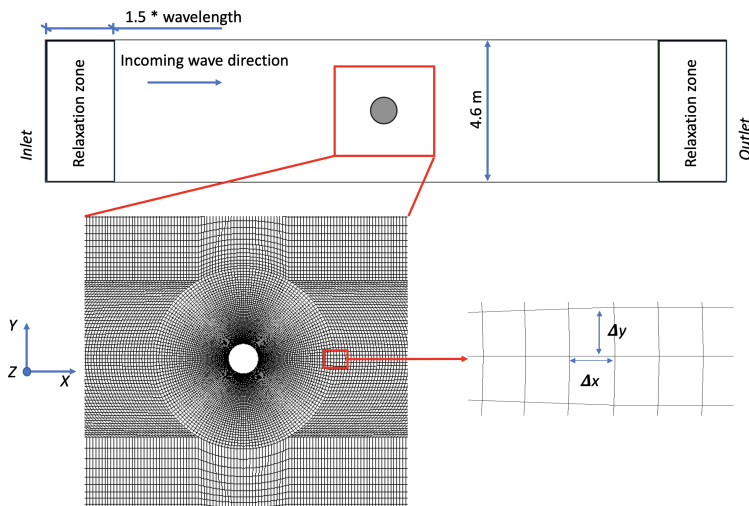


FIGURE 3. Top view of the numerical wave tank and mesh layout around the cylinder in the XY plane.

4. Methodology

4.1. Three phase decomposition method

Four-phase decomposition is based on the form of Stokes expansions in both wave amplitude and frequency. The idea is that by running an experiment four times with the phase of the wave field changed from the original by 90° , 180° , 270° , then the principle sum harmonic contributions can be extracted by linear combinations of the phase shifted signals.

We modify the four-phase decomposition method discussed in previous studies (Fitzgerald *et al.* 2014; Feng *et al.* 2020) to predict the harmonic components of force ($F_{1,2,3,4,5}$) based only on three of the four phases in the decomposition method. The new idea is that if an additional non-linear process beyond that expected from a Stokes-type expansion (perhaps additional loading from wave breaking) is triggered in only one of the four phases we can use the other three phases to make a prediction of the loads in the fourth phase without the additional non-linearity and thus isolate the load due to the additional non-linear process. Let us suppose the additional non-linear process occurs in the 0 degree case \mathbb{F}_0 . We can then re-construct what the total force time history of \mathbb{F}_0 phase would be if the additional local force had not occurred. The three-phase harmonic extraction (using $\mathbb{F}_{90,180,270}$) can be written as:

$$\begin{aligned}
 AF_1 - A^4 F_4 + A^5 F_5 + O(A^6) &= -\frac{1}{4} (\mathbb{F}_{90} + 2\mathbb{F}_{180} + \mathbb{F}_{270} + \mathbb{F}_{90}^H - \mathbb{F}_{270}^H) \\
 A^2 F_2 - A^4 F_4 + O(A^6) &= -\frac{1}{2} (\mathbb{F}_{90} + \mathbb{F}_{270}) \\
 AF_1 - A^3 F_3 + A^5 F_5 + O(A^7) &= \frac{1}{2} (-\mathbb{F}_{90}^H + \mathbb{F}_{270}^H).
 \end{aligned} \tag{4.1}$$

where the H superscript is the Hilbert transform of the time series. The predicted time series for the 0 degree case is then compared against the 0 degree case measured in the experiment and the differences indicate the additional ‘strongly non-linear’ process beyond that expected from a Stokes-type expansion in force.

Figure 4 (a) shows that, for a steep wave group without any strong non-linearity

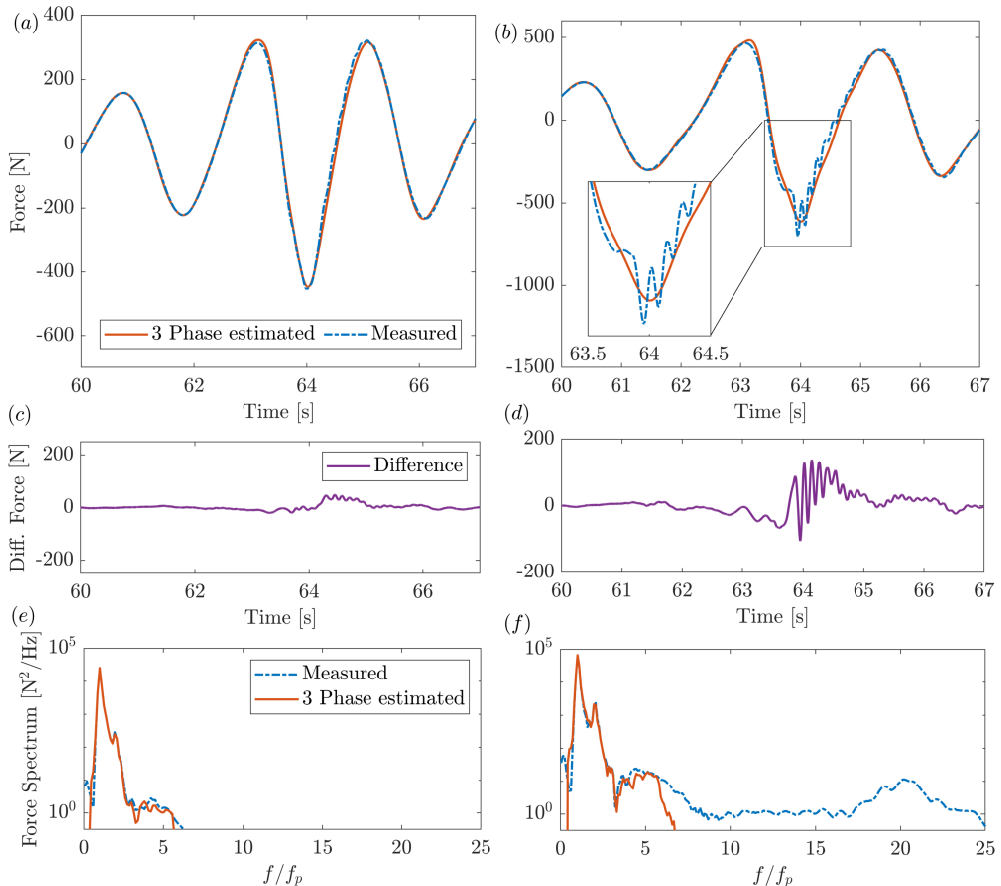


FIGURE 4. Three-phase reconstruction of the 4th phase prediction of total diffracted nonlinear forces (a): a steep wave group without secondary load cycle ($Ak_p = 0.17$, $k_p R = 0.12$), (b): a wave group with resonance structure response associated with secondary load cycle (case 1, $Ak_p = 0.18$, $k_p R = 0.12$), (c – d) show the force difference between the three-phase decomposition prediction and the measured force in the experiment for these two wave groups and (e – f) show the corresponding force energy spectrum with logarithmic scale on the vertical axis.

measured in the experiment, the proposed three-phase decomposition method recreates the total harmonic force accurately. For wave groups with additional nonlinear forces beyond the Stokes-type model, the proposed three-phase decomposition method allows the identification of those nonlinear forces beyond the wave loading from the Stokes-type model. As shown in Figure 4 (b), the three-phase decomposition method separates the secondary load cycle and structural responses from the Stokes harmonics cleanly at the trough of the force time series and agrees well with the measured force elsewhere. This can also be confirmed in Figure 4 (c – d), where the difference between the three-phase decomposition predicted force and the measured nonlinear force in the experiment are presented. We subtract the three-phase estimated signal from the measured forces during the experiment to obtain the difference. The additional non-linear process beyond that expected from a Stokes-type expansion (i.e. the force associated with the high frequency resonant response) is isolated from the measured nonlinear force, which can be further confirmed by the force spectral plots shown in Figure 4 (e – f).

4.2. High-frequency force analysis with wavelets

We further investigate the spatial-temporal energy distribution of the loading by an isolated wave group using wavelet analysis. Similar approaches have been widely used in extreme wave grouping, wave breaking detection and characterisation, and also wave structure impact characterisation (Massel 2001; Derakhti & Kirby 2016; Liberzon *et al.* 2019). We follow Derakhti & Kirby (2016) for the construction of a continuous wavelet transform $M_F(s, t)$ of the discrete sequence of the measured inline force series $F(t)$ on the cylinder with a scaled and translated mother wavelet ϕ given as:

$$E_F(s, t) = \frac{1}{\sqrt{s}} \int_{-\infty}^{\infty} F(\tau) \phi^* \left(\frac{\tau - t}{s} \right) d\tau, \quad (4.2)$$

where t is time, $s = (\theta_w f)^{-1}$ is the scale factor which dilates the signals when $s < 1$ and compresses the signal when $s > 1$, $\theta_w = 4\pi / \left(\omega_0 + \sqrt{2 + \omega_0^2} \right)$ is a constant associated with the Fourier wavelength of the mother wavelet ϕ , $F(\tau)$ is defined as the convolution of $F(t)$, τ is the translation factor, and $*$ denotes the complex conjugate. The mother wavelet we adopt is the commonly used Morlet wavelet $\phi(t) = e^{i\omega_0 t} e^{-(t^2/2)}$ (Farge 1992), where the ω_0 is the nondimensionalised central frequency of the mother wavelet.

In Figure 5 (a), we show the wavelet scalogram of the three-phase predicted force, which shows the clear structure of higher-order harmonics. The wavelet scalogram also shows almost zero magnitude for frequencies that are higher than $7f_p$ (see the bottom panel of Figure 5 (a)). The measured force including the non-Stokes-like component (in Figure 5 (b)), however, shows clear additional peaks above $7f_p$, which are not consistent with the Stokes type higher harmonics model. Similar energy re-distribution into the high-frequency range can also be seen in Figure 4 (e – f), although the time distribution of energy is unresolved in the spectrum. Structural resonance at the natural frequency of the test rig can be triggered during the experiments due to the high-frequency energy content of the quasi-impulsive loading. We remove the structural resonance responses following the frequency response method (Chen *et al.* 2018), and apply a response transfer function in the frequency domain. The natural frequency and damping ratio of the system are determined by the damped free vibration curve from a hammer test. We find that the structural responses are only significant at frequencies that are close to the natural frequency.

We subtract the wavelet scalogram of the three-phase estimated signal from the measured scalogram during the experiment to obtain the difference between these two plots in Figure 5 (c)), which demonstrates the magnitude change due to the presence of the quasi-impulsive force and the associated secondary load cycle. We observe a magnitude reduction in the linear and second-order sum-harmonics frequency range over a slightly longer time and a sharp magnitude gain in a wide range of high frequencies happening over a very short time interval. This quasi-impulsive energy gain in high frequencies is superficially similar to the energy increase reported during slamming impacts (Esandi *et al.* 2020). This difference between the measured force and the three-phase predicted force indicates the strong nonlinear effects (i.e. the secondary load cycle and the associated backwards quasi-impulsive forcing) cause extra energy transfer from low frequencies to a wide range of high frequencies in a short period of time.

4.3. Wave run-up on the cylinder with image processing

The four-camera system in our experiments provides a set of synchronised views of the scattered wave field from different angles. In this study, we analysed in detail the video captured by the side camera. An example of a frame captured by this camera is

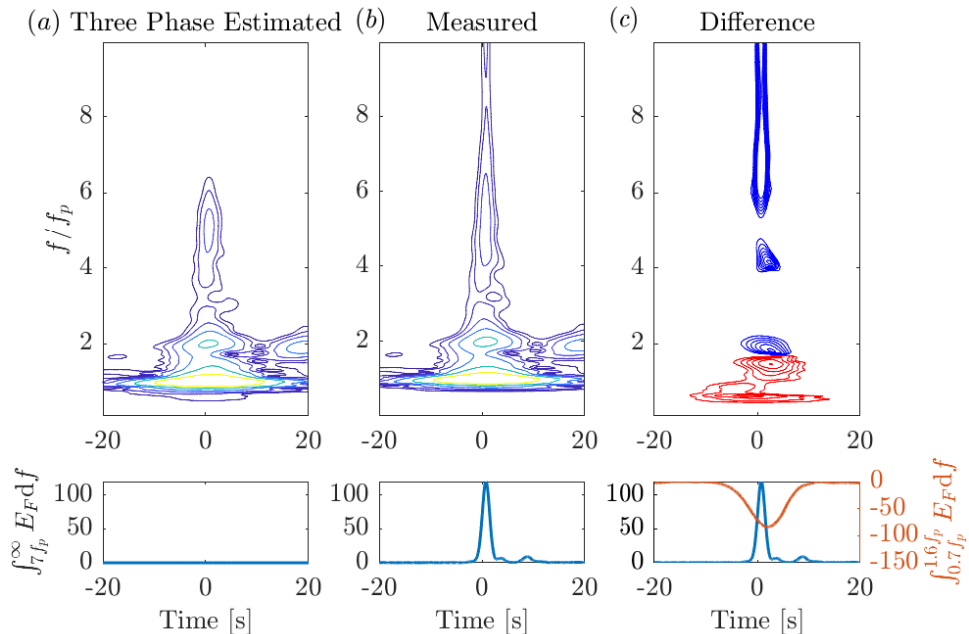


FIGURE 5. Wavelet analysis of total diffracted inline force series of case 1 for three-phase reconstruction (left), measured inline force (middle), the contours are varying from 2.6 (in blue) to 110 (in yellow) in \log_{10} scale. The difference (measured - 3-phase reconstructed) between the two wavelet scalograms (right), the blue contour shows positive differences and the red contour shows negative differences. Both contours vary from 2.6 to 8 with a linear scale. The units for wavelet amplitude is $N\sqrt{\text{Hz}}$. In the bottom panels, we present the integrated wavelet scalogram increase for force components with frequency content larger than $7f_p$ in blue and the integrated wavelet scalogram reduction in the linear region in red (i.e. between $0.7f_p$ and $1.6f_p$), where f_p is peak frequency.

shown in Figure 6. We deployed standard camera calibration and check-board detection procedures (Zhang 2000). We first detected the edges of each checkboard rectangle with a corner detection algorithm, where the locations with significant image intensity value variation in multiple directions are labelled. The intrinsic and extrinsic parameters of the camera can be estimated based on these identified corner points.

The wave run-up points (i.e. the air-water boundary) on the cylinder are extracted manually for every frame that is close to the focus time of the wave group. The camera parameters determined in the calibration stage are then used to accurately interpret the image by matching the pixel coordinates to the real-world coordinates. The still water level is determined by processing frames at the start of the experiment when the flume is free of waves.

We present the validation case here in Figure 6, where we applied the image processing method to a quasi-linear experimental case, where we expected minimal nonlinear wave run-up and wave scattering at the shoulder point (i.e. the most outer point of the cylinder in the transverse direction of the incoming wave field). The captured run-up profile matches well to the empty tank surface elevation time-history from a wave gauge at the same location, excluding the presence of what we interpret as the Type-II wave scattering, as shown in Figure 6 (d).

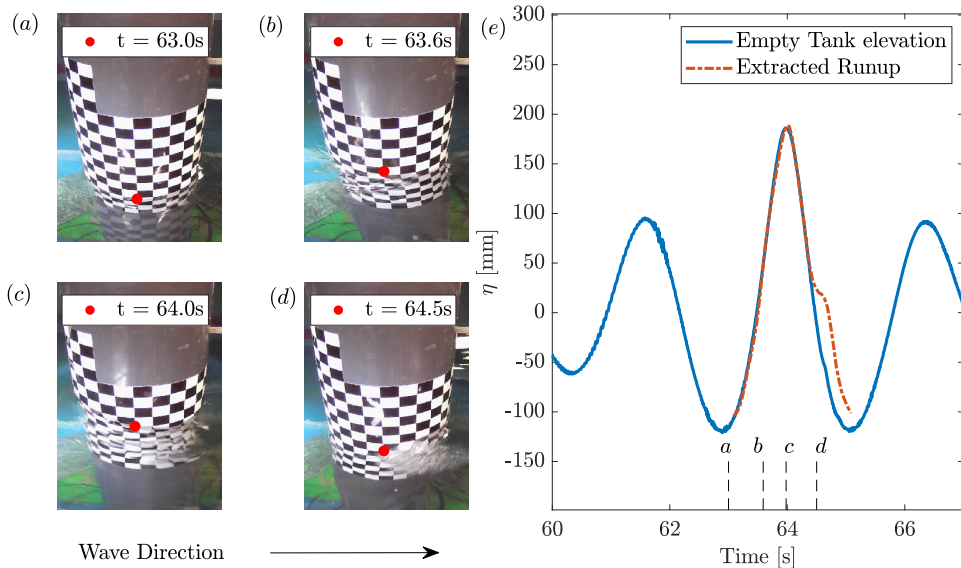


FIGURE 6. Validation results for our image processing approach on wave run-up. (a – d): the wave run-up profile on the cylinder with red dot indicating the run-up point at the centre of the cylinder. Arrow indicates the incoming wave direction. (e): wave run-up profile compared against surface elevation without cylinder. Dashed lines indicate the time instances of the photo from a to d.

5. Results

5.1. Occurrence of secondary load cycle and structural response

We first investigate the occurrence of the quasi-impulsive loading over 200 wave group experimental runs. We present the experimental results in Figure 7 with the horizontal axis showing the nondimensionalised incoming wave steepness and the vertical axis the nondimensional cylinder radius.

We have also included reference lines for a Froude number which has been found to be a good predictor of a secondary load cycle (Grue *et al.* 1993). Recent studies also suggest this extra nonlinear loading can occur at short waves outside the flow separation regime Antoloni *et al.* (2020). The two lines are at $Fr = 0.3$ and $Fr = 0.4$. We have another line for $Fr = 0.45$ as a predictor of the backwards quasi-impulsive loading with details explained further at the end of this section. Following Riise *et al.* (2018b), we estimate the Froude number as:

$$Fr = 2\pi\eta_c/T_p\sqrt{gD}, \quad (5.1)$$

where η_c is the maximum surface elevation measured from the empty tank results at the centre of the cylinder, T_p is the peak wave period, g is the gravitational acceleration and $D = 2R$ is the cylinder diameter.

We identify the secondary load cycle following the method presented in Riise *et al.* (2018b), where the high-frequency force signals above $3.5f_p$ are manually investigated. We find the Froude number with a threshold roughly between 0.3 and 0.4 can separate the cases into those with a secondary load cycle on the right of the Froude number curve, and those without to the left. Our results are consistent with previous studies (Grue & Huseby 2002; Chang *et al.* 2019). This is also shown in Figure 7.

For the occurrence of this quasi-impulsive wave force, we found it challenging to find a simple and straightforward way of identifying these occurrences directly from the inline

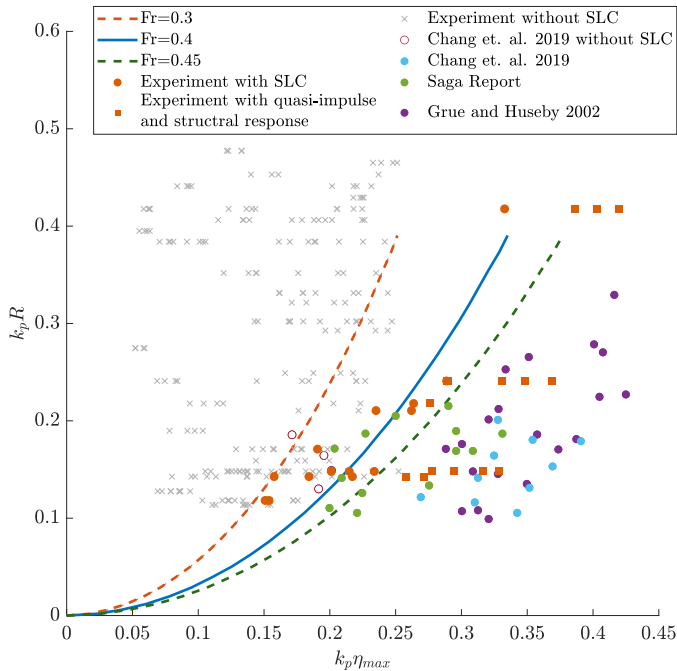


FIGURE 7. Occurrence of the secondary load cycle (SLC) and structural response compare against previous results reported by Saga Petroleum (1995); Grue & Huseby (2002); Chang *et al.* (2019), and Fr number is calculated following Riise *et al.* (2018b)

force time series. As such, we manually examine the wavelet scalogram and label those cases with this extra impulse. We identify this quasi-impulsive force with a significant energy contribution above $7f_p$ after removing the force components due to the structural response following the frequency response method in Chen *et al.* (2018).

From Figure 7, we report that the extra quasi-impulsive force does not always take place when a secondary load cycle appears during the experiment. Instead, the occurrences of these quasi-impulsive forces require higher wave steepness or more slender cylinders when compared to the cases with only the secondary load cycle, which also roughly follow the Froude number scaling with a higher threshold of around 0.45 (also shown in Figure 7). We also identify structural resonance as a clear energy peak around the natural frequency of the structure (8 Hz), which also closely follows the occurrence of the secondary load cycle. We observe clear structural resonance for all the cases with this quasi-impulsive force in the current experimental setup, which suggests a strong interconnection between these two processes. However, we note that this observation is not directly applicable to the structural resonance in the field as the response characteristics of the systems in the laboratory scale are very different from those in the field scale

5.2. Wave nonlinear run-up and scattering

We further investigate the source of this quasi-impulsive backwards loading starting from the wave run-up on the cylinder. Based on the image processing method outlined in Section 4.3, we first present the run-up time histories at the shoulder of the cylinder (i.e. the most outer point of the cylinder in the transverse direction of the incoming wave field) for numerical simulations and experimental observations in Figure 8. For

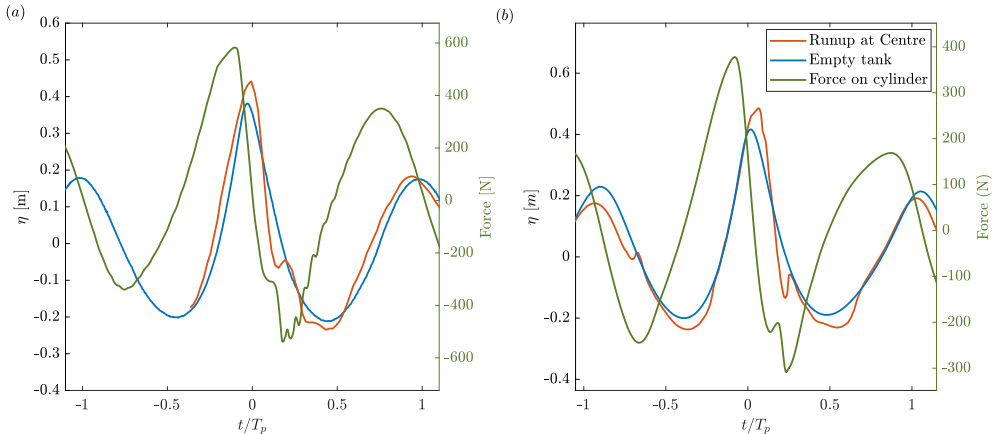


FIGURE 8. Comparison between the wave run-up at the shoulder (i.e. the most outer point of the cylinder in the transverse direction of the incoming wave field) of the cylinder (red), surface elevation measured at the cylinder centre but without cylinder (blue) and total diffracted inline force (green) for (a) experimental results (case1) and (b) numerical simulations (case3).

both cases, the wave run-up time histories show a clear localised peak after the main wave crest presumably due to the wave scattering around the cylinder. We also observe an alignment in time between this localised peak and the quasi-impulsive force, both of which occur at $0.3T_p$ after the maximum force peak.

We further explore the localised peak in the run-up associated with the wave scattering field captured during experiments, as shown in figure 9(e). We compare the run-up time series with the empty tank surface elevation, and both of these profiles agree well, though with two main differences. These two departures are consistent in both the experiments and numerical simulations using OpenFOAM. Firstly, the run-up profile on the cylinder is higher than the empty tank elevation at the crest of the wave. This is due to a thin water sheet run-up projected upwards on the surface of the cylinder, as shown in Figure 9(c). This is consistent with previous numerical studies (Chen & Zhao 2022). The localized peak in a shorter time scale is caused by a Type-II scattered wave travelling in the opposite direction to the incoming wave. This wave will travel around the cylinder, and the scattering of this wave in the latter stages is consistent with the Type-II scattering reported previously by Swan & Sheikh (2015).

We present the spatial-temporal wave run-up profile in Figure 10, where the Type-II scattering is initially formed at the back of the cylinder and travels around the body perimeter towards the front stagnation point. As this local wave disturbance moves, it introduces local maxima in the run-up profiles. The pink plane on the figure indicates the time when the quasi-impulsive force is measured in the experiment, which is close to the time when the Type-II scattered wave was first detected in the run-up. We report comparable sizes of runup on the upstream and downstream sides within the view angle of our synchronised camera system in the experiment. This trend is consistent with numerical simulation results, and the large runup from the downstream side of the cylinder has been previously reported by Ghadirian & Bredmose (2020) with numerical simulations and also from experiments by Kristiansen & Faltinsen (2017).

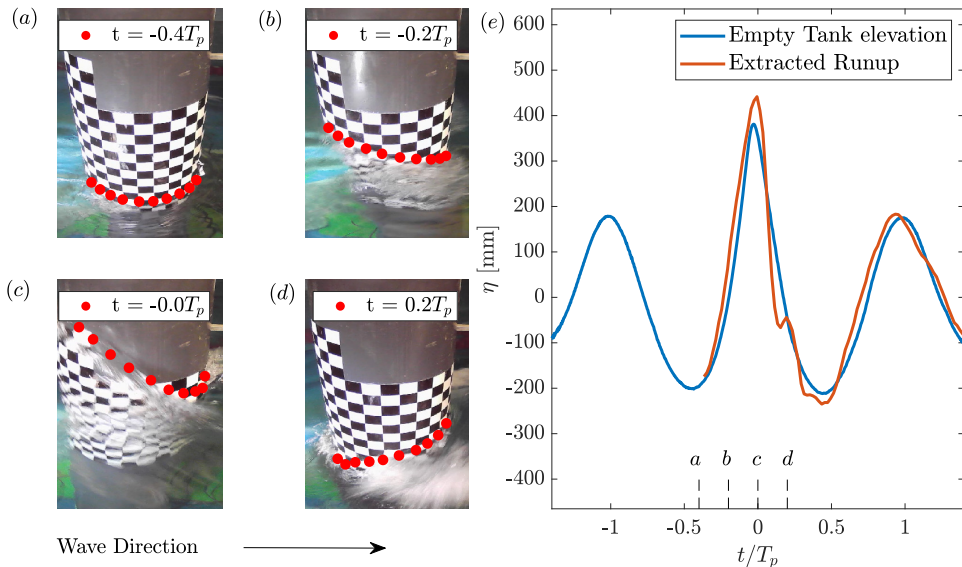


FIGURE 9. (a – d): Wave run-up profile for case 1 on the cylinder with red dots indicating the run-up point around the cylinder. Arrow indicates the incoming wave direction. (e): wave run-up profile for case 1 at the shoulder point of the cylinder (i.e. the most outer point of the cylinder in the transverse direction of the incoming wave field) (red) compared against the surface elevation measured at the cylinder centre but without cylinder (blue). The empty tank surface elevation (blue) corresponds to the red and blue lines in Figure 8 (a). Dashed lines indicate the time instances of the photo from a to d.

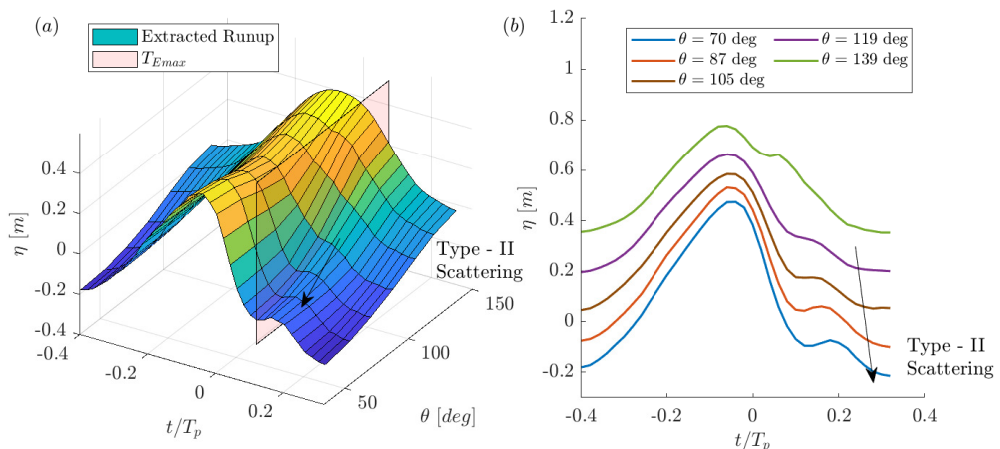


FIGURE 10. Wave run-up profile on the cylinder for case 1 with (a) spatial-temporal evolution with red plane indicating the time instant (T_{Emax}) when the wavelet scalogram shows a peak for high frequency force ($f > 7f_p$), and (b) cross section planes of spatial-temporal profile at various positions along the cylinder. $\theta = 0$ for the front stagnation point and $\theta = 180$ for the rear stagnation point of the cylinder. Each line is separated by 0.1 m starting from the $\theta = 70$ case. The wave group we analysed here has peak period of $T_p = 2.5$ s and wave steepness at linear focus of $k_p A = 0.175$ and $k_p R = 0.147$.

5.3. Backwards forces estimation with impact model

To further investigate the time correlation between the appearance of the Type-II scattered wave and the quasi-impulsive backwards force, we track the motion of the Type-II scattered wave around the cylinder with the maximum local run-up points. We present the time when the local run-up profile reaches a localised maximum ($T_{\eta,c}$) for different locations on the cylinder in Figure 11 (a). The nondimensionalised position of different observation nodes along the x direction is shown on the vertical axis with the circumferential angle in the colour gradient. The x is defined as the projected distance along the tank centreline, and a positive value of x indicates the rear side of the cylinder.

The local maximum run-up point first appears close to the rear point of the cylinder and agrees well with the observations reported by Kristiansen & Faltinsen (2017). In addition to this gradual process, we also observe the local maximum run-up point suddenly accelerates, traveling at a faster speed towards the front side of the cylinder. This suggests a faster-moving wave (i.e. the Type-II scattered wave) appears from the rear side of the cylinder and propagates in the opposite direction to the incoming wave. More importantly, this sudden acceleration of the local maximum run-up point coincides with the time when the quasi-impulsive force occurs and can also be clearly seen in the wavelet scalogram in Figure 11 (b). This suggests the arrival of the Type-II scattered wave is closely connected to the quasi-impulsive force observed experimentally. Also, the secondary local cycle seems to start at earlier (i.e. when wave run-up reaches the maximum near the rear stagnation point) and moves initially away with a much slower propagation speed. This difference in the time scales suggests that the quasi-impulsive force we discussed here could potentially be caused by a different underlying physical process from the typical secondary load cycle discussed in the literature.

We now investigate the entire scattering wave field in the vicinity of the cylinder at the time instant when this quasi-impulsive force occurs, as shown in Figure 12. The numerical simulation results for scattered wave field are presented in Figure 12 (a) with the empty tank elevation subtracted to remove the influence of the undisturbed incident wave. In Figure 12 and also videos in the supplementary materials, localised ‘white caps’ can be observed at the back of the cylinder with a rough scattered wave field, and the splashing of the water with a significant amount of air entrainment is superficially similar to the classic wave breaking processes. We also observed an evident initial engagement of the Type-II scattered wave with the rear side of the cylinder, which was further confirmed by the videos captured by the side view camera during the experiment (see supplementary materials for details). Similar observations on the scattered wave field profiles are also reported by Ghadirian & Bredmose (2020) with numerical simulations and also from experiments by Kristiansen & Faltinsen (2017).

Finally, we adapt a classic wave impact model to demonstrate the time correlation between the Type-II scattered wave and the quasi-impulsive force in the reverse direction. We focus on this backward quasi-impulsive force at the later stage of the secondary load cycle and the impact model discussed in this study does not capture the initial part of the secondary load cycle. The aim here is to build a practical model for approximating this force which captures the essential elements. The model assumes the infinite lateral width of the impacting wave crest and a curling factor to capture the shape of the rolling break. The ambiguity in these assumptions may affect the quantitative estimation of the impact magnitude, but not the impact time calculations which is the key objective here. The latter primarily depends on the speed of the wave and the geometry of the cylinder, both of which can be estimated directly from numerical simulations and experiments with the run-up profile.

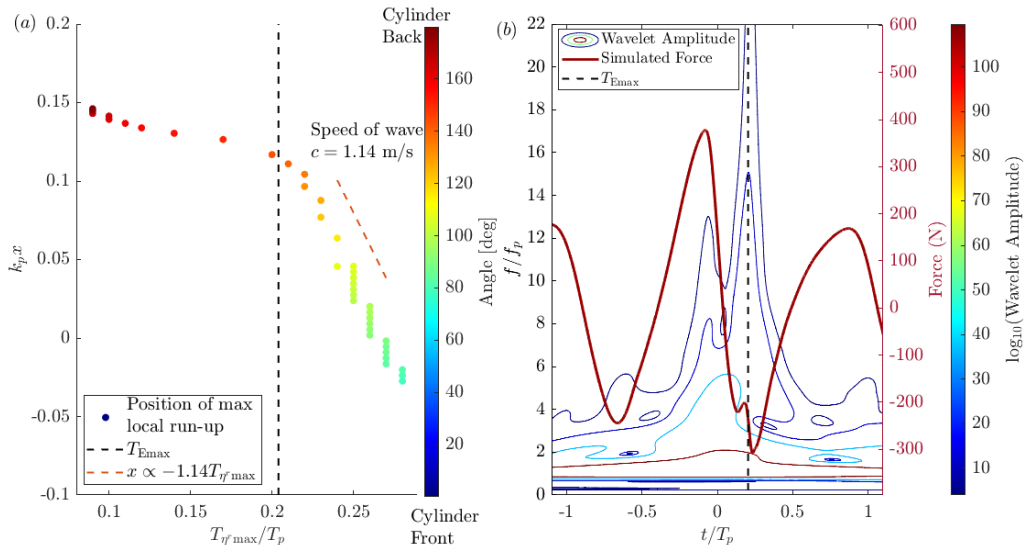


FIGURE 11. (a): The locations of sampling points along the cylinder for case 3 against the arrival time of the Type-II scattered wave (calculated as the time when run-up reaches a local maximum at each sampling point). The black dash line indicates the time T_{Emax} instant when the wavelet scalogram shows a peak for high-frequency force ($f > 7f_p$). The red line shows the slope of the linear fitted line used to calculate the speed of the wave. (b): the combined plot of the wavelet scalogram and the corresponding total inline force profile. The black dash line indicates the time T_{Emax} instant when the wavelet scalogram shows a peak for high frequency force ($f > 7f_p$). The nondimensionalised kR value of the cylinder radius is 0.147 in the presented case. x is defined as the projected distance along the tank centreline, and a positive value of x indicates the rear side of the cylinder.

The quasi-impulsive impact from locally breaking waves on a vertical cylinder may be modelled using various versions of the wave impact model (eg, Von Karman (1929); Wagner (1932); Ghadirian & Bredmose (2019)). In this study, we apply one of the most commonly used breaking wave models based on the work of Goda (1966) to the new quasi-impulsive force acting backwards against the wave propagation direction. This is formulated as:

$$F_I(t) = \lambda \eta_b C_s \rho R c^2 \left(1 - \frac{c}{R} t\right), \quad (5.2)$$

where λ is the wave curling factor, η_b the crest height of the incoming wave, c is the wave celerity, ρ is the fluid density, C_s is the impact coefficient and R is the cylinder radius. The values of some of the coefficients are given in Table 2. From Table 2, the impact time, which can be estimated as R/c , is very small. This agrees well with the observation that this new quasi-impulsive force has a very short duration from the wavelet analysis.

To adopt the classic wave impact model, we estimate the impact crest height (η_b) as the difference between the measured run-up height and the empty tank undisturbed wave field (i.e. $\Delta\eta$ in Figure 12 (a)). The wave celerity (c) can be directly calculated as the gradient of the $x - t$ plot shown in Figure 11 (a). For the other terms, such as impact coefficients, curling factor, and impact time formulation, we use standard values (Goda 1966) shown in Table 2 without any further modification. We present the prediction of this quasi-impulsive force based on the Type-II scattered wave in figure 13. We used the three-phase decomposition method to remove any nonlinear force beyond the Stokes expansion for both the experimental cases (a, b) and one numerical simulation case (d) in figure 13. For the numerical simulation results in panel (c), where the three phase

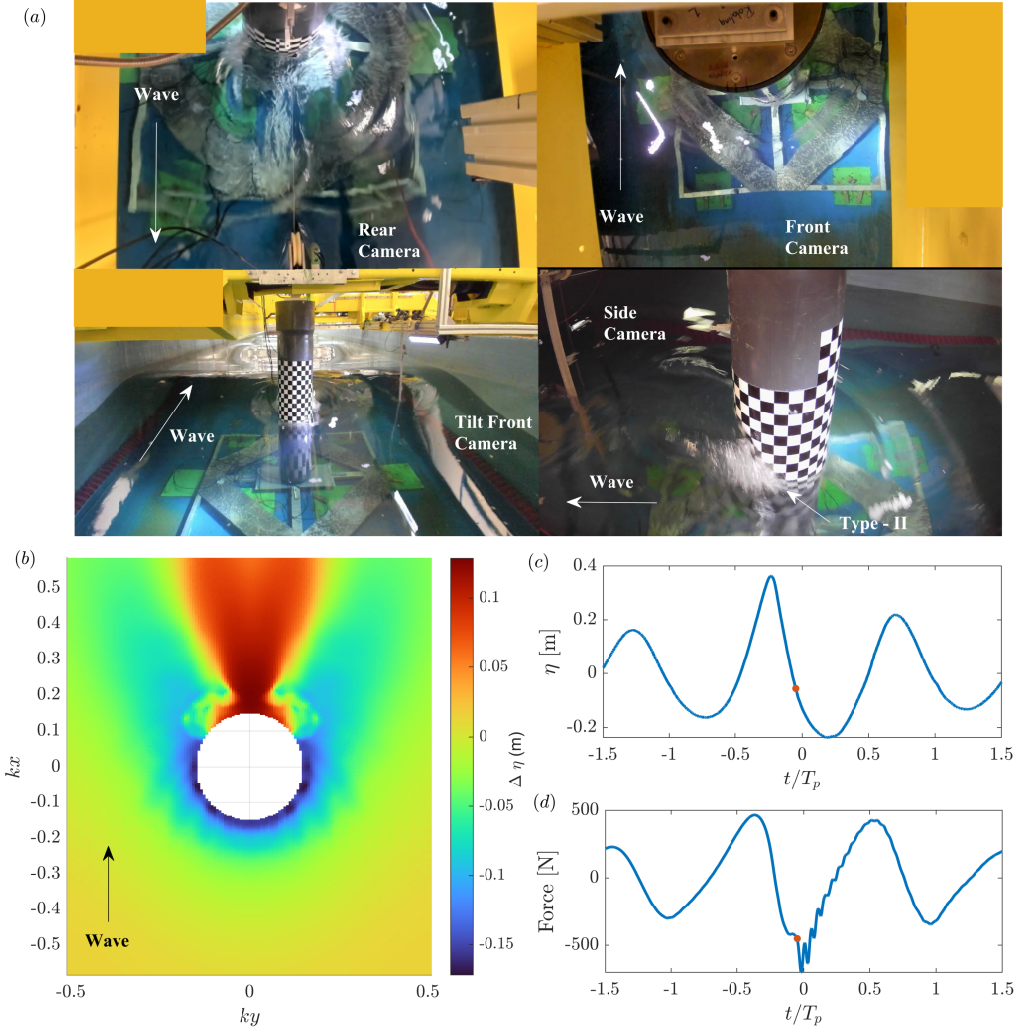


FIGURE 12. Wave scattering field at the time when high-frequency forces impact first occur for (a) experimental results (case 3) with the empty tank surface elevation in (c) and total inline force in (d), and (b) shows numerical simulation (case 1). Red dots indicate the current time of the plot. Video versions of both experimental and numerical results are provided in the supplementary material.

decomposition is not applicable due secondary load cycle appearing in multiple phases, we utilise a low-pass filter at $2.4f_p$ to remove the nonlinear force associated with impact and secondary load cycle following Riise *et al.* (2018b).

We recover the local inline force by superimposing an impact in the opposite direction to the incoming wave, which leads to better agreement between the measured force and both the numerical simulations and experiments. However, this additional load component does not capture the secondary load cycle, as the phenomenon occurs before the impact. Unsurprisingly, the proposed impact model cannot accurately capture the magnitude of this negative impact, primarily because the underlying mechanism and behaviour of the Type-II scattered wave are distinct from the typical incoming breaking wave hitting an obstacle. For example, as shown in Figure 7, this Type-II scattered wave forms a crescent shape and only affects the scattered wave field within the first $0.5 R$ of

TABLE 2. Values used for the impact model. The peak impact crest height is obtained as the difference between the measured run-up height and the empty tank undisturbed wave field (i.e. $\Delta\eta$ in Figure 12 (a)) and the crest speed is obtained based on the slope in Figure 11. The (a – d) notation corresponds to the values measured for two experimental results (cases 1, 2) and two numerical simulation results (cases 3, 4) respectively, which are also presented in Figure 13 (a – d).

Name	Value
Curling factor λ	0.4
Impact coefficient C_s	π
Cylinder radius R	0.2 m
Peak Impact Crest Height $\Delta\eta$	(a) 0.32 m (b) 0.308 m (c) 0.134 m (d) 0.24 m
Crest speed c	(a) 1.36 m/s (b) 1.18 m/s (c) 1.14 m/s (d) 1.06 m/s

the cylinder. Nevertheless, the fact that this simplified breaking model can recover most of the characteristics of this quasi-impulsive force, particularly with accurate arrival time estimations, suggests a strong correlation between the Type-II scattered wave and this backwards impact.

6. Discussion and Conclusions

In this paper, we investigate a new loading component in the form of a quasi-impulsive force acting in the opposite direction to the incoming waves, which is associated with the secondary load cycle. To identify this new force, we utilize a novel three-phase decomposition method to separate nonlinear forces beyond the main Stokes-type expansion, as well as the wavelet transform to explore the frequency-time energy distribution. We confirm that this backwards force, which occurs right after the secondary load cycle, has somewhat similar characteristics to a classic breaking wave impact at the crest of the wave. A significant amount of high-frequency energy is identified at the impact time across a wide range of frequencies, which can be clearly observed up to $20 f_p$ in the wavelet scalogram in the log scale.

We further investigate the spatio-temporal evolution of the wave run-up profile on the cylinder and use a classic wave impact model to examine the interconnections between the run-up and the nonlinear quasi-impulsive force. The strong time correlation match between the occurrence of this quasi-impulsive force and the arrival of Type-II scattered wave suggests that the scattered wave is likely to be the source of this nonlinear force in the opposite direction. Because of the complexity of the violent scattered field on the rear side of the cylinder, we found it challenging to rule out all other potential causes of this quasi-impulsive force on the cylinder. For example, a head-on collision of disturbances around the back of the cylinder would lead to a similar impact but should take place slightly earlier. However, from the observation that we are able to approximate this impulse with a simplified impact model without further modification for 4 different cases (2 physical experiments and two in CFD), we are confident that the impact from the Type-II scattered wave contributes to the impulse we identified.

We hope this work sheds some light on the secondary load cycle phenomenon as the quasi-impulsive force appears to happen right after it. As mentioned in the introduction, this impulsive force is generally considered a part of the secondary load cycle in previous

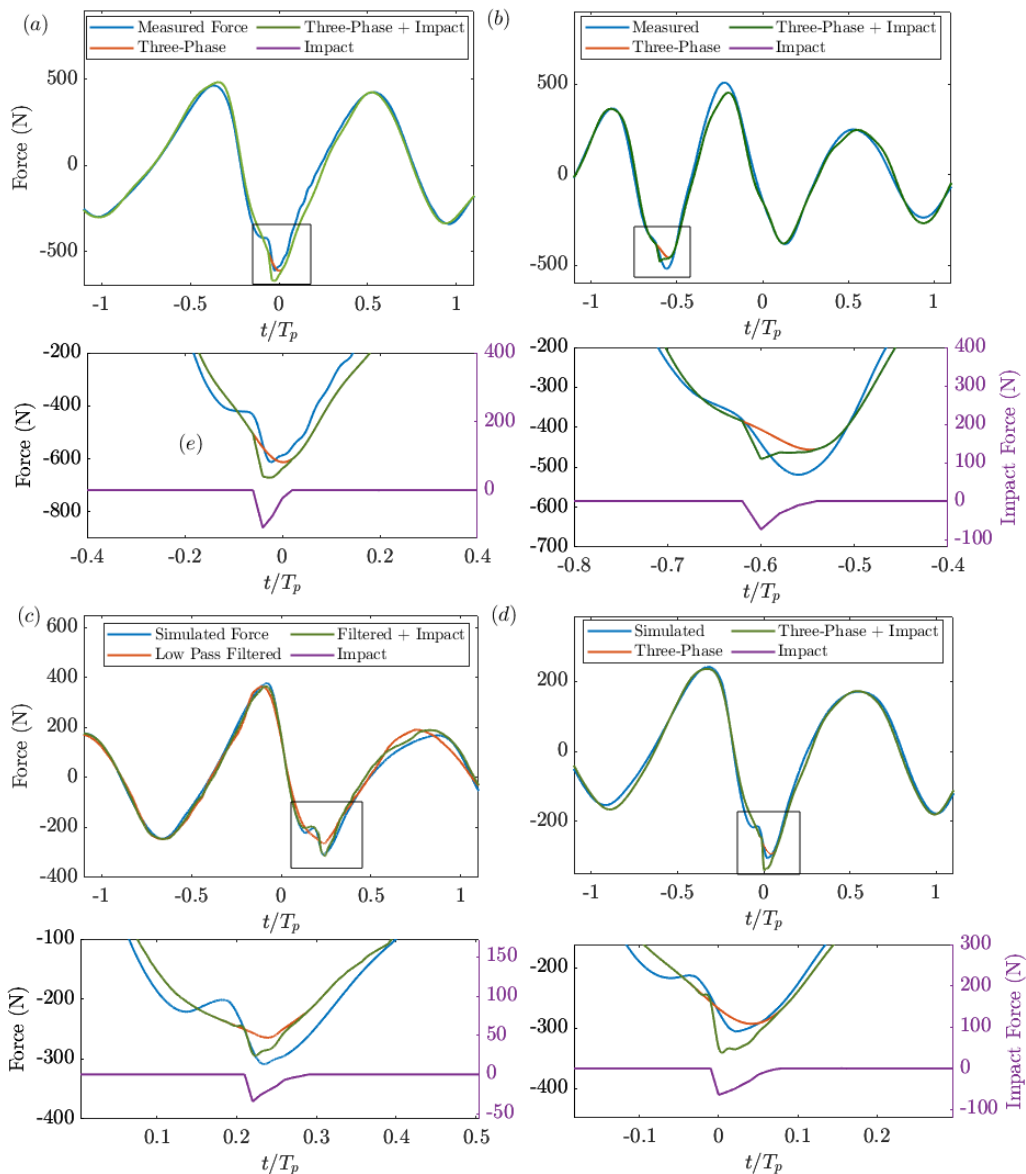


FIGURE 13. Comparison of measured total inline forces(blue), three-phase reconstruction or low-pass filtered (at $2.4f_p$) estimated inline forces without high-frequency loading (red) and the linear combination of three-phase predicted force with impact loading estimated from the Goda impact model (green) for (c, d): numerical simulations (case 3, 4), (a, b): experimental results (case 1, 2). The bottom panel shows a zoom in view of (a – d) around the trough with the backwards impact force estimated by the Goda impact model (Goda 1966).

literature where some common characteristics have been described. In line with this perspective, our findings are in agreement with numerous prior investigations, including the notable amplification of energy observed in the fourth and fifth harmonics reported by Kristiansen & Faltinsen (2017), as well as the interpretation of the secondary load cycle as a prominent non-linear phenomenon in Rainey (2007). However, our results suggest a hypothesis of multiple underlying physical processes contributing to the secondary load

cycle with different time scales and durations. We explored the faster-travelling Type-II scattered wave which arrives later in the timeline with an extremely short duration. Prior to this backward impulsive force, the local maximum run-up on the cylinder suggests a slower underlying process, which contributes to the initial rise of the secondary load cycle. This slow-rising process is not covered by the current study and deserves further investigation.

We would also like to discuss the limitations of our study. Due to the physical constraints of the experimental facility, our quantitative analysis is restricted to the wave run-ups on the cylinder, and we only have qualitative data available for the entire wave scattering field in the experimental results. This limitation unfortunately presents significant challenges when investigating the initial part of the secondary load cycle. Another limitation of this study is that we only consider unidirectional wave fields, which differ from the spread wavefields in the open ocean. Although we have limited insights into how the quasi-impulsive force would behave in spread seas, we believe that our unidirectional results serving as a limiting case will still provide valuable insights into the underlying physics.

In this study, we focused on the hydrodynamic force on a fixed vertical cylinder, which is the first step towards a better understanding of the subsequent structural responses during the secondary load cycle. Some evidence, however, has indicated that this impulsive force is also important for the subsequent structural responses. We observe clear structural resonance at the natural frequency (so often called ringing responses) for all the cases with this quasi-impulsive force present for the entire experimental campaign (see Figure 7). Unfortunately, the current experimental setup limits further assessment of the response effect for several reasons. Firstly, the structural dynamics characteristics are very different for the test rig ($20\times$ of peak wave frequency) and for those of the offshore wind turbine ($2-3\times$ of peak wave frequency (Schl er *et al.* 2016)). Secondly, the current laboratory scale is also very different from the field scale. As such, further studies are required with flexible supported cylinders or large-scale numerical simulations to examine the impact of this quasi-impulsive force on the subsequent structural responses.

Finally, we would like to discuss the implications of this study. Our results provide a possible explanation for the question—why the secondary load cycle associated structural resonance phenomenon persists even if the natural frequency of the system is set to be tens of times higher than the wave frequency ($20\times$ higher in our experiments). It seems that the excitation of the structural resonance by the secondary load cycle shares a very similar underlying process with that due to wave breaking at crest: a short-duration quasi-impulsive event excites the system at its natural frequency. One significant difference, however, is the impulsive event from the secondary load cycle is in the opposite direction to the incoming wave. This new and unexpected impact direction requires further attention in future offshore designs, as wave impacts are previously believed to be predominantly aligned with the mean wave direction. Our study here also suggests an additional physical process to be considered when predicting the wave impacts on the monopile foundations and similar cylindrical supporting structures: in addition to the well-known breaking wave impact, the nonlinear scattered wave field can also lead to a quasi-impulsive impact, which happens at a much lower wave steepness than these wave breaking events.

Acknowledgement

This research is funded by EPSRC grant EP/V050079/1. TT is also funded by Eric and Wendy Schmidt AI in Science Postdoctoral Fellowship. An abbreviated version of

this work was recently reported at IWWF38. We thank Profs John Grue, Trygve Kristiansen and Henrick Bredmose for their comments on the work at the workshop. We thank Prof. Rodney Eatock Taylor for his detailed comments and intriguing discussions with the authors. This research was funded in whole or in part by EPSRC grant number EP/V050079/1. For the purpose of Open Access, the author has applied a CC BY public copyright licence to any Author Accepted Manuscript (AAM) version arising from this submission.

Declaration of interests

The authors report no conflict of interest.

Author Credit Statement

Tianning Tang: Conceptualization, Methodology, Experiment, Software, Validation, Formal analysis, Data curation, Writing – original draft, Visualization. Haoyu Ding: Investigation, Experiment, Writing – review & editing. Saishuai Dai: Experiment, Investigation. Jun Zang: Methodology, Resources, Experiment, Writing – review & editing, Supervision, Funding acquisition. Paul H. Taylor: Conceptualization, Methodology, Supervision, Data curation, Writing – review & editing. Thomas A. A. Adcock: Methodology, Resources, Writing – review & editing, Supervision, Project administration, Funding acquisition. ”

REFERENCES

- ADCOCK, T A A & TAYLOR, P H 2009 Focusing of unidirectional wave groups on deep water: an approximate nonlinear Schrödinger equation-based model. *Proc. R. Soc. A Math. Phys. Eng. Sci.* **465** (2110), 3083 LP – 3102.
- ANTOLLONI, G, JENSEN, A, GRUE, J, RIISE, B H & BROCCINI, M 2020 Wave-induced vortex generation around a slender vertical cylinder. *Phys. Fluids* **32** (4), 042105.
- BALDOCK, T E, SWAN, C & TAYLOR, P H 1996 A laboratory study of nonlinear surface waves on water. *Philos. Trans. Royal Soc. A Math. Phys. Eng. Sci.* **354** (1707), 649–676.
- CHANG, S, HUANG, W, SUN, H & LI, L 2019 Numerical investigation of secondary load cycle and ringing response of a vertical cylinder. *Appl. Ocean Res.* **91**, 101872.
- CHAPLIN, J R, RAINEY, R C T & YEMM, R W 1997 Ringing of a vertical cylinder in waves. *J. Fluid Mech.* pp. 119–147.
- CHAPLIN, J. R., SUBBIAH, KESAVAN & IRANI, MEHERNOSH 1992 Local forces on a vertical cylinder in regular and irregular waves. *Int. Offshore Polar Eng. Conf.* pp. ISOPE–I–92–270.
- CHAPLIN, J. R., SUBBIAH, K. & IRANI, M. 1995 Loading on a Vertical Cylinder in Multidirectional Waves. *J. Offshore Mech. Arct. Eng.* **117**, 151–158.
- CHAPLIN, JOHN R., SUBBIAH, KESAVAN & IRANI, MEHERNOSH B. 1993 Effects of wave directionality on the in-line loading of a vertical cylinder. *Int. Offshore Polar Eng. Conf.* pp. ISOPE–I–93–235.
- CHAU, F P & EATOCK TAYLOR, R 1992 Second-order wave diffraction by a vertical cylinder. *J. Fluid Mech.* **240**, 571–599.
- CHELLA, M A, TØRUM, A & MYRHAUG, D 2012 An overview of wave impact forces on offshore wind turbine substructures. *Energy Procedia* **20**, 217–226.
- CHEN, L F, ZANG, J, HILLIS, A J, MORGAN, G C J & PLUMMER, A R 2014 Numerical investigation of wave-structure interaction using openfoam. *Ocean Eng.* **88**, 91–109.
- CHEN, L F, ZANG, J, TAYLOR, P H, SUN, L, MORGAN, G C J, GRICE, J, ORSZAGHOVA, J & RUIZ, M T 2018 An experimental decomposition of nonlinear forces on a surface-piercing column: Stokes-type expansions of the force harmonics. *J. Fluid Mech.* **848**, 42–77.

- CHEN, S & ZHAO, W 2022 On the scattering of focused wave by a finite surface-piercing circular cylinder: A numerical investigation. *Phys. Fluids* **34** (3), 035132.
- CHOI, SUNG-JIN, LEE, KWANG-HO & GUDMESTAD, OVE TOBIAS 2015 The effect of dynamic amplification due to a structures vibration on breaking wave impact. *Ocean Eng.* **96**, 8–20.
- DERAKHTI, M & KIRBY, J T 2016 Breaking-onset, energy and momentum flux in unsteady focused wave packets. *J. Fluid Mech.* **790**, 553–581.
- EATOCK TAYLOR, R & HUNG, S M 1987 Second order diffraction forces on a vertical cylinder in regular waves. *Appl. Ocean Res.* **9** (1), 19–30.
- ESANDI, J M, BULDAKOV, E, SIMONS, R & STAGONAS, D 2020 An experimental study on wave forces on a vertical cylinder due to spilling breaking and near-breaking wave groups. *Coast. Eng.* **162**, 103778.
- FALTINSEN, O M, NEWMAN, J N & VINJE, T 1995 Nonlinear wave loads on a slender vertical cylinder. *J. Fluid Mech.* **289**, 179–198.
- FARGE, M 1992 Wavelet transforms and their applications to turbulence. *Annu. Rev. Fluid Mech.* **24** (1), 395–458.
- FENG, X, TAYLOR, P H, DAI, S, DAY, A H, WILLDEN, R H J & ADCOCK, T A A 2020 Experimental investigation of higher harmonic wave loads and moments on a vertical cylinder by a phase-manipulation method. *Coast. Eng.* **160**, 103747.
- FITZGERALD, C J, TAYLOR, P H, EATOCK TAYLOR, R, GRICE, J & ZANG, J 2014 Phase manipulation and the harmonic components of ringing forces on a surface-piercing column. *Proc. R. Soc. A* **470** (2168), 20130847.
- GHADIRIAN, A & BREDMOSE, H 2019 Pressure impulse theory for a slamming wave on a vertical circular cylinder. *J. Fluid Mech.* **867**, R1.
- GHADIRIAN, A & BREDMOSE, H 2020 Detailed force modelling of the secondary load cycle. *J. Fluid Mech.* **889**, A21.
- GODA, Y 1966 A study on impulsive breaking wave force upon a vertical pile. *Rept. Port and Harbour Res. Inst.* **5** (6), 1–30.
- GRUE, JOHN 2002 On four highly nonlinear phenomena in wave theory and marine hydrodynamics. *Appl. Ocean Res.* **24**, 261–274.
- GRUE, J, BJØRSHOL, G & STRAND, Ø 1993 Higher harmonic wave exciting forces on a vertical cylinder. *Preprint series. Mechanics and Applied Mathematics, Matematisk Institutt, Universitetet i Oslo* .
- GRUE, J, BJØRSHOL, G, STRAND, Ø & OHKUSU, M 1994 Nonlinear wave loads which may generate ‘ringing’ responses of offshore structures. In *IWWFEB*, , vol. 17, p. 55.
- GRUE, J & HUSEBY, M 2002 Higher-harmonic wave forces and ringing of vertical cylinders. *Appl. Ocean Res.* **24** (4), 203–214.
- HUSEBY, M & GRUE, J 2000 An experimental investigation of higher-harmonic wave forces on a vertical cylinder. *J. Fluid Mech.* **414**, 75–103.
- JACOBSEN, N G, FUHRMAN, D R & FREDSOE, J 2012 A Wave Generation Toolbox for the Open-Source CFD Library: OpenFoams. *Int. J. Numer. Meth. Fluids* **70** (9), 1073–1088.
- KIM, M-H & YUE, DICK K P 1989 The complete second-order diffraction solution for an axisymmetric body part 1. monochromatic incident waves. *J. Fluid Mech.* **200**, 235–264.
- KRISTIANSEN, T & FALTINSEN, O M 2017 Higher harmonic wave loads on a vertical cylinder in finite water depth. *J. Fluid Mech.* **833**, 773–805.
- KROKSTAD, J. R., STANSBERG, C. T., NESTEGARD, A. & MARTHINSEN, T. 1998 A new nonslender ringing load approach verified against experiments. *J. Offshore Mech. Arct. Eng.* **120** (1), 20–29.
- LEE, S., KIM, M., KO, K. & HONG, J. 2021 Nondimensionalized semi-empirical equation to predict secondary load cycles on vertical cylinders of different diameters. *Ocean Eng.* **230**, 108968.
- LI, J, ZHANG, H, LIU, S, FAN, Y & ZANG, J 2022 Experimental investigations of secondary load cycle formation in wave force on a circular cylinder under steep regular waves. *Ocean Eng.* **253**, 111265.
- LIBERZON, D, VREME, A, KNOBLER, S & BENTWICH, I 2019 Detection of breaking waves in single wave gauge records of surface elevation fluctuations. *J. Atmos. Oceanic Technol.* **36** (9), 1863–1879.
- LIU, JIAWANG & TENG, BIN 2023 Spectral wave explicit weak-scattering approach for higher

- harmonic wave loads and ringing response of flexible monopile. *Appl. Ocean Res.* **130**, 103415.
- LO, E & MEI, C C 1985 A numerical study of water-wave modulation based on a higher-order nonlinear Schrödinger equation. *J. Fluid Mech.* **150**, 395–416.
- MA, L & SWAN, C 2020 An experimental study of wave-in-deck loading and its dependence on the properties of the incident waves. *J. Fluids Struct.* **92**, 102784.
- MA, L & SWAN, C 2023a An experimental study of wave-in-deck loading and its dependence on the properties of the topside structure. *Marine Struct.* **88**, 103340.
- MA, L & SWAN, C 2023b Wave-in-deck loads: an assessment of present design practice given recent improvements in the description of extreme waves and the nature of the applied loads. *Ocean Eng.* **285**, 115302.
- MACCAMY, R C & FUCHS, R A 1954 *Wave forces on piles: a diffraction theory*. US Beach Erosion Board.
- MALENICA, Š & MOLIN, B 1995 Third-harmonic wave diffraction by a vertical cylinder. *J. Fluid Mech.* **302**, 203–229.
- MARTHINSEN, T., STANSBERG, C.T. & KROKSTAD, J.R. 1996 On the ringing excitation of circular cylinders. *Int. Offshore Polar Eng. Conf. All Days*, ISOPE-I-96-030.
- MASSEL, S R 2001 Wavelet analysis for processing of ocean surface wave records. *Ocean Eng.* **28** (8), 957–987.
- MASTERTON, S & SWAN, C 2006 Wave forces on a single surface-piercing column: Comparisons between theory and experiment. In *OMAE*, , vol. 47470, pp. 383–391.
- MJ, D, MCALLISTER, M L, BREDMOSE, H, ADCOCK, T A A & TAYLOR, P H 2023 Harmonic structure of wave loads on a surface piercing column in directionally spread and unidirectional random seas. *J. Ocean Eng. Mar. Energy*. pp. 1–19.
- NEWMAN, J N 1996 Nonlinear scattering of long waves by a vertical cylinder. *Wave Nonlinear Process Hydrodyn.* pp. 91–102.
- PAULSEN, B T, BREDMOSE, H, BINGHAM, H B & JACOBSEN, N G 2014 Forcing of a bottom-mounted circular cylinder by steep regular water waves at finite depth. *J. Fluid Mech.* **755**, 1–34.
- RAINEY, R C T 2007 Weak or strong nonlinearity: the vital issue. *J. Eng. Math.* **58** (1), 229–249.
- RIISE, B H, GRUE, J, JENSEN, A & JOHANNESSEN, T B 2018a High frequency resonant response of a monopile in irregular deep water waves. *J. Fluid Mech.* **853**, 564–586.
- RIISE, B H, GRUE, J, JENSEN, A & JOHANNESSEN, T B 2018b A note on the secondary load cycle for a monopile in irregular deep water waves. *J. Fluid Mech.* **849**, R1.
- SAGA PETROLEUM 1995 Report for saga petroleum. higher order wave loads on a vertical column. MT51-F95-0139.
- SAINCHER, S, SRIRAM, V, AGARWAL, S & SCHLURMANN, T 2022 Experimental investigation of hydrodynamic loading induced by regular, steep non-breaking and breaking focused waves on a fixed and moving cylinder. *Eur. J. Mech. B/Fluids.* **93**, 42–64.
- SCHLØER, S, BREDMOSE, H & BINGHAM, H B 2016 The influence of fully nonlinear wave forces on aero-hydro-elastic calculations of monopile wind turbines. *Mar. Struct.* **50**, 162–188.
- SHEIKH, R & SWAN, C 2005 Wave slamming on vertical surface-piercing cylinders: the role of nonlinear wave scattering. In *Proc. ISOPE*. OnePetro.
- STANSBERG, C.T., HUSE, E., KROKSTAD, J.R. & LEHN, E. 1995 Experimental Study of Non-Linear Loads On Vertical Cylinders In Steep Random Waves. *Int. Ocean Polar Eng. Conf.* pp. ISOPE-I-95-013.
- STANSBERG, C T 1997 Comparing ringing loads from experiments with cylinders of different diameters - an empirical study. *International conference on the behaviour of offshore structures, Delft (Netherlands), 7-10 Jul 1997* .
- SWAN, C, MASTERTON, S, SHEIKH, R & CAVALLETTI, A 2005 Wave forcing and wave scattering from a vertical surface-piercing cylinder. In *OMAE*, , vol. 41960, pp. 571–580.
- SWAN, C & SHEIKH, R 2015 The interaction between steep waves and a surface-piercing column. *Phil. Trans. R. Soc. A* **373** (2033), 20140114.
- TANG, TIANNING, RYAN, GERARD, DING, HAORYU, CHEN, XI, ZANG, JUN, TAYLOR, PAUL H & ADCOCK, THOMAS AA 2024 A new gaussian process based model for non-linear wave loading on vertical cylinders. *Coast. Eng.* **188**, 104427.

- TAYLOR, PH, TANG, T, ADCOCK, TAA & ZANG, J 2024 Transformed-FNV: Wave forces on a vertical cylinder—A free-surface formulation. *Coast. Eng.* **189**, 104454.
- TROMANS, P, SWAN, C & MASTERTON, S 2006 Nonlinear potential flow forcing: the ringing of concrete gravity based structures. *Health and Safety Executive Report, UK* .
- VON KARMAN, T 1929 The impact on seaplane floats during landing. *National Advisory Committee on Aeronautics, Washington, DC., National Advisory Committee on Aeronautics* .
- WAGNER, H 1932 Uber stob-und gleitvorgange an der oberflache von flussigkeiten. *Z Angew Math Mech.* **12**, 193–215.
- WANG, Y., XU, F. & ZHANG, Z. 2020 The secondary load cycle of a bottom-mounted circular cylinder at different keulgan-carpenter numbers and froude numbers. *Ocean Eng.* **213**, 107675.
- YOUNG, I 2020 Wind-generated waves. In *Ocean Dyn.*, pp. 1–20.
- ZANG, JUN, TAYLOR, PAUL H, MORGAN, GERALD, STRINGER, ROBERT, ORSZAGHOVA, JANA, GRICE, JAMES & TELLO, M 2010 Steep wave and breaking wave impact on offshore wind turbine foundations—ringing re-visited. In *25th IWWWFB*, pp. 9–12.
- ZHANG, Z. 2000 A flexible new technique for camera calibration. *IEEE Trans. Pattern Anal. Mach. Intell.* **22** (11), 1330–1334.